

PCCP

Accepted Manuscript



This is an *Accepted Manuscript*, which has been through the Royal Society of Chemistry peer review process and has been accepted for publication.

Accepted Manuscripts are published online shortly after acceptance, before technical editing, formatting and proof reading. Using this free service, authors can make their results available to the community, in citable form, before we publish the edited article. We will replace this *Accepted Manuscript* with the edited and formatted *Advance Article* as soon as it is available.

You can find more information about *Accepted Manuscripts* in the [Information for Authors](#).

Please note that technical editing may introduce minor changes to the text and/or graphics, which may alter content. The journal's standard [Terms & Conditions](#) and the [Ethical guidelines](#) still apply. In no event shall the Royal Society of Chemistry be held responsible for any errors or omissions in this *Accepted Manuscript* or any consequences arising from the use of any information it contains.



PCCP

ARTICLE

Nanocrystalline anatase TiO₂/reduced graphene oxide composite films as photoanodes for photoelectrochemical water splitting studies: the role of the reduced graphene oxide

Received 00th January 20xx,
Accepted 00th January 20xx

DOI: 10.1039/x0xx00000x

www.rsc.org/

Andreia Morais,^a Claudia Longo,^a Joyce R. Araujo,^b Monica Barroso,^c James R. Durrant,^d Ana Flavia Nogueira^{*a}

Nanocrystalline TiO₂ and reduced graphene oxide (TiO₂/RGO) composite films were prepared by combining sol-gel method with hydrothermal treatment, employing titanium isopropoxide (Ti(OⁱPr)₄) and graphene oxide (GO) as starting materials. Although several reports in the literature explore the benefits of RGO addition in titania films for photocatalysis and water splitting reactions, the role of RGO in the composite always stands as a material that is able to act as an electron acceptor and transport electrons more efficiently. However, in most of the reports, no clear evidences for such "role" are presented, and the main focus is deviated to the improved efficiency and not to the reasons for. In this work, we employed several techniques to definitively present our understanding of the role of the RGO in titania composite films. The TiO₂/RGO composites films were characterized by X ray diffraction, Raman spectroscopy, microscopy and electrochemical techniques. In the photoelectrochemical water splitting studies, the TiO₂/RGO_(0.1%) photoelectrodes showed the highest photocurrent density values (0.20 mA cm⁻² at 1.23 V_{RHE}) compared to other electrodes, with an increase of 78 % in relation to the pristine TiO₂ films (0.11 mA cm⁻² at 1.23 V_{RHE}). The transient absorption spectroscopy (TAS) results indicated an increase in lifetime and yield of both photogenerated holes and electrons. Interesting, the TiO₂/RGO_(0.1%) films was the one which exhibited the best charge generation upon excitation, corroborating with the photoelectrochemical data. We proposed that in films with lower concentration (< 0.1 wt %), the RGO sheets are electron acceptors, and a decrease in the charge recombination processes is the immediate consequence. Thus, both holes and electrons live longer and contribute more effectively to the photocurrent density .

Introduction

Since Fujishima and Honda¹ (1972) reported for the first time the photoelectrochemical water splitting into hydrogen (H₂) and oxygen (O₂) over titanium dioxide or titania (TiO₂) photoanodes, different kinds of semiconductors have been developed and evaluated as candidate photoelectrodes for solar-driven hydrogen production.² Among the diversity of semiconductors, the TiO₂ is still one of the more studied as photocatalyst, due to its excellent thermal, chemical and photochemical stability, insolubility in water and availability in

large scale. The photoactivity of this material is observed only when it is irradiated with ultraviolet light, which corresponds to only approximately 4 % of incident solar energy.³ Many strategies to improve the absorption in the visible part of the solar spectrum were accomplished: introduction of impurities (e.g. nitrogen atoms) to change its band gap⁴ and sensitization with particles as CdS, CdSe or CdTe.⁵ The development of new architectures such as nanotubes⁶, nanowires⁷, nanorods⁸ and nanoparticles⁹ is also an alternative to improve its performance by increasing the semiconductor surface area and/or electronic transport.

Another challenge for the more efficient use of TiO₂ as photocatalyst for water splitting or pollutants oxidation is to improve the electronic transport that occurs by diffusion in the oxide semiconductor film.¹⁰ In this case, the diffusion of the photogenerated charge carriers is relatively "slow" on conventional TiO₂ films and hence, the charge recombination probability increases, resulting in a decrease in the photocurrent density and photocatalytic efficiency for several reactions.¹¹ An interesting alternative to reduce this effect is by the incorporation of carbon-based materials into nanocrystalline TiO₂ films, such as carbon nanotubes¹², carbon black¹³ and carbon quantum dots¹⁴. Our group has demonstrated with success the use of boron or nitrogen-

^a Chemistry Institute, University of Campinas (UNICAMP), P. O. Box 6154, 13083-970, Campinas, São Paulo, Brazil.

^b National Institute of Metrology, Quality and Technology, Av. Nossa Sra. das Graças, 50, 25250-020, Duque de Caxias, Rio de Janeiro, Brazil.

^c Debye Institute for Nanomaterials Science, Utrecht University, Bolognalaan 10 VII, 3584 CJ Utrecht, Netherlands.

^d Department of Chemistry, Imperial College London, South Kensington Campus, London SW7 2AZ, United Kingdom.

Electronic Supplementary Information (ESI) available: [Synthesis of reduced graphene oxide and its characterization by XRD, Raman, XPS, TGA, FEG-SEM and HRTEM; characterization of TiO₂ and TiO₂/RGO films by optical microscopy and UV-vis spectroscopy; electrochemical properties of these films by Cyclic Voltammetry, Chronoamperometry and Electrochemical Impedance Spectroscopy and IPCE analysis]. See DOI: 10.1039/x0xx00000x

doped hollow carbon in TiO₂(P25) films for photoelectrochemical studies¹⁵ and TiO₂/MWCNT as photoanodes in dye sensitized solar cells.¹⁶ Other carbonaceous material that has been widely used for this application is the graphene, due to high surface area (2630 m² g⁻¹), photodegradation resistance, optical transparency (~ 97.7 %) and high charge mobility values (200,000 cm² V⁻¹ s⁻¹).¹⁷

The graphene derivative, graphene oxide (GO) is an electrically insulating material and usually exhibits a rich assortment of oxygen-containing groups such as carboxylic, hydroxyl, carbonyl, and epoxide groups. The electrical conductivity of GO can be increased by reduction and partial restoration of the sp²-hybridized network, then the resulting product, also known as reduced graphene oxide (RGO), has properties similar to graphene (although the reduction methods do not fully restore the ideal characteristics of the graphene sheets).^{18,17}

Nevertheless, the combination between TiO₂ nanoparticles and RGO sheets remains a good strategy to improve the photocatalytic performance of the semiconductor oxide for several reactions. The electron-accepting ability presented by RGO sheets can be used to enhance electron transport properties in the TiO₂ films.¹⁹⁻²² For instance, Ng *et al.*²³ reported that the TiO₂(P25)-RGO nanocomposite electrodes showed significant activity for the photocatalytic decomposition of 2,4-dichlorophenoxyacetic acid and Bell *et al.*²⁴ proposed the use of these nanocomposite films for photoelectrochemical water splitting. The researchers observed a significant increase in the photocurrent density value compared to pure TiO₂ film, for all wavelengths in the ultraviolet region. Li and Cui²⁵ observed that TiO₂/RGO (0.2 wt%) reached a hydrogen production rate of 43.8 μmol h⁻¹, which is 1.6 times greater than for the TiO₂ sample. Recently, our research group demonstrated that the presence of RGO in TiO₂/CdS films can increase the methanol production from the photoreduction of carbon dioxide (CO₂)²⁶ while, in TiO₂/Cu₂O films may favor the photocatalytic degradation of the methylene blue dye.²⁷ In addition, films of TiO₂/RGO applied as electron transport layers improved the efficiency of P3HT/PC₆₁BM organic solar cells.²⁸ Although the advantages of RGO sheets incorporation in the TiO₂ matrix are widely disseminated, unfortunately, a detailed understanding about the role of graphene and its derivatives is still very controversial and scarce in the literature. Some studies suggest that the RGO can facilitate electron injection and assist in the electron transport^{29, 30}, while other works reported that the RGO can act as a sensitizer in the semiconductor oxide films.³¹⁻³³ For this reason, there is a need for a more detailed and definitive investigation of the role of the RGO sheets in the TiO₂ matrix, and how such successful combination of materials has improved the photocatalytic performance of several oxides.

Herein, we report a facile route for the growth of nanocrystalline TiO₂ particles on RGO sheets by combining sol-gel method with hydrothermal treatment, employing titanium isopropoxide (Ti(OⁱPr)₄) and graphene oxide (GO) as starting materials. In the photoelectrochemical water splitting studies,

the influence of the addition of different amounts of RGO in the TiO₂ matrix was investigated by Cyclic Voltammetry, Chronoamperometry and Electrochemical Impedance Spectroscopy (EIS) analysis. Charge generation/recombination dynamics (electrons and holes) using transient absorption spectroscopy (TAS) was also employed to correlate the excited state dynamics with the electrochemical reactions at the photoanode.

Experimental

Material

All reagents were of analytical grade and used without further purification. The natural graphite powder was purchased from *Nacional de Grafite* LTDA (code: Micrograf 99507UJ). All other reagents were purchased from Sigma-Aldrich. The fluorine-doped tin oxide (FTO) conductive glasses (Hartford glass, R_s ≤ 10 Ω sq⁻¹) were cleaned ultrasonically with water-detergent solution, water, acetone, methanol and isopropanol successively in ultrasonic baths for 15 min. All substrates were dried with compressed nitrogen gas and treated with UV-ozone for 20 min.

Preparation of nanocrystalline TiO₂/RGO pastes

The synthesis of reduced graphene oxide (RGO) from graphite and its characterization by XRD, Raman, TGA, FEG-SEM and HRTEM were described in the Supporting Information (Figs. S2-S6, Tables S1, S2). In the Supporting Information, a detailed characterization of the graphite and graphene oxide (precursors in the synthesis of the RGO sheets) is also available. Besides, X ray photoelectron analyses (XPS) were used to determine the chemical composition of the graphite, graphene oxide and RGO-hydrothermal samples. The pastes containing nanocrystalline TiO₂ particles and RGO (TiO₂/RGO) were prepared, using the titanium isopropoxide (Ti(OⁱPr)₄) and GO as starting materials. Firstly, the 1.8 % w/w GO dispersion (5.8 g) was dispersed in 0.10 mol L⁻¹ HNO₃ solution (100 mL) using ultrasonic bath for 30 min. Meanwhile, glacial acetic acid (3.5 mL) was added to Ti(OⁱPr)₄ (16 mL) under stirring in a closed system previously purged with nitrogen. The TiO₂ precursors were then injected into the acid GO dispersion, heated and maintained at 80 °C for 8 h in reflux; after the suspension was autoclaved at 220 °C for 12 h. Finally, using a rotary evaporator, the resulting homogeneous suspension was concentrated to a colloidal paste, comprised of 11 wt % nanocrystalline TiO₂ particles and 5.0 wt % of RGO (designed as TiO₂/RGO_(5%)). After that, polyethylene glycol (PEG, Mw = 2000) was added in a proportion of 40 % of the total TiO₂ weight.

Also, a TiO₂ paste was prepared by the same procedure in the absence of RGO. Pastes containing different relative amount of RGO, TiO₂/RGO_(0.01%), TiO₂/RGO_(0.05%), TiO₂/RGO_(0.1%), TiO₂/RGO_(0.5%), TiO₂/RGO_(1%) and TiO₂/RGO_(2%) were prepared using adequate amounts of the TiO₂/RGO_(5%) and the TiO₂ pastes (see Fig. S1 in the Supporting Information). The resulting pastes were stored in a screw-threaded glass bottles.

Preparation of TiO₂/RGO Films

For the preparation of the electrodes, an aliquot of the TiO₂ or TiO₂/RGO paste was spread onto the fluorine-doped tin oxide conductive substrate (glass-FTO) by the doctor blading technique, using adhesive tape (Scotch Magic Tape, 3 M, thickness < 50 μm) to control film thickness. After drying in air for 30 min, the films were heated at 350 °C for 2 h, with a heating rate of 10 °C min⁻¹. The resulting films were uniform, without any noticeable cracks; the average thickness, measured with a Taylor/Hobson Form Talysurf 50 profilometer. These samples were cut into 1 × 1.5 cm² pieces, resulting in electrodes with geometrical active area of 1.0 cm². These electrodes were stored in a dry atmosphere.

Characterization of TiO₂/RGO Films

X ray diffraction (XRD) measurements were performed using a Shimadzu XRD7000 diffractometer (40 kV, 30 mA) with Cu (λ = 1.541 78 Å) irradiation in the 2θ range of 5°-80°. The Raman spectra were obtained in a confocal Raman spectrometer (model T64000 – Jobin Yvon – USA), equipped with a CCD (charge coupled device) detector and an Olympus BTH 2 microscope. The excitation laser was set at 514 nm with a 20-fold magnification objective lens.

Optical microscopy images were taken with a Nikon Eclipse 5i (H5505, Nikon, Japan) microscope equipped with Digital Sight Camera System (DS-Fi1 Nikon, Japan) and using an objective lens with a magnification of 20 ×. Field emission gun scanning electron microscopy (FEG-SEM) images were taken on a FEI Inspect F50 microscope at a voltage of 10 kV. High-resolution transmission electron microscopy (HRTEM) images were conducted using a JEM 3010 URP microscope at an accelerating voltage of 300 kV.

Photoelectrochemical Studies of TiO₂/RGO Films

Electrochemical measurements were carried out in an Autolab[®] model PGSTAT 10N potentiostat/galvanostat (Eco Chemie). The electrochemical impedance spectroscopy (EIS) measurements were carried out in an Autolab[®] model PGSTAT-302-N potentiostat/galvanostat with frequency response analyzer FRA module (Eco Chemie). The EIS measurements were done at the open circuit potential with a sinusoidal voltage perturbation of 10 mV, in the frequency range from 50 kHz to 5 mHz.

A conventional three-electrode photoelectrochemical cell, consisting of a glass-FTO|TiO₂ or glass-FTO|TiO₂/RGO as working electrodes (active area of 1 cm²), a platinum wire as counter electrode and Ag/AgCl in a KCl solution (3.0 mol L⁻¹) as reference electrode, was used in the experiments. An aqueous H₂SO₄ solution (0.5 mol L⁻¹) was used as electrolyte. The measured E_{Ag/AgCl} potentials values were converted to the reversible hydrogen electrode potentials (E_{RHE}), using the Nernst equation and considering the standard potential of the reference electrode, E⁰_{Ag/AgCl}, which corresponds to 0.21 V_{RHE} at 25 °C:

$$E_{\text{RHE}} = E_{\text{Ag/AgCl}}^0 + E_{\text{Ag/AgCl}} + 0.059 \text{ pH} \quad \text{Eq. 1}$$

The photoelectrochemical cell was placed in an optical bench consisting of an Oriol Xe (Hg) 250 W lamp coupled to an AM 1.5G filter (Oriol) and collimating lenses. The light intensity was calibrated with an optical power meter; model 1830-C (Newport) to 100 mW cm⁻², but no correction was made to discount reflection and transmission losses.

Transient Absorption Spectroscopy

The investigation of the recombination dynamics of the photogenerated electrons and holes in the TiO₂ and TiO₂/RGO films was performed using transient absorption spectroscopy (TAS). All transient absorption measurements in the μs-s time scale were performed using a Nd:YAG laser (Continuum Surelite I-10) as a source the UV excitation source (355 nm, ~ 200 μJ cm⁻² / pulse, typically 1 Hz repetition rate and 6 ns pulse width). A 75 W xenon lamp (Hamamatsu) was used as continuous light source (probe beam). The lamp wavelengths were selected, using a monochromator, at 460 nm and 900 nm for lifetime monitoring of the photogenerated holes and electrons, respectively. The second monochromator after the sample was used to reduce the emission intensity and scattering from the laser before reaching the Si PIN photodiode. The detection system was comprised of a silicon photodiode (Hamamatsu Photonics) coupled to a digital oscilloscope (Tektronix TDS220) triggered by the laser excitation pulse. The transient decay data is the result of averaging between 300 laser shots. The TiO₂ and TiO₂/RGO films were placed in a sealed quartz cuvette and were thoroughly degassed with nitrogen prior to use. In this work, ΔOD means the transient absorption change.

Results and discussion

Structural and morphological properties of TiO₂ and TiO₂/RGO nanoparticles and films

The morphological characterization of the TiO₂ and TiO₂/RGO materials was investigated through FEG-SEM and HRTEM. Fig. 1(a) shows that TiO₂ particles have varied sizes and shapes, with an average diameter of ~15 nm. These features were also observed in the composite samples with different RGO concentration. For the TiO₂/RGO composite, HRTEM and FEG-SEM images indicate that the RGO sheets are completely covered and decorated by TiO₂ nanoparticles (Fig. 1(b to d)). Such strong interaction between the RGO sheets and the TiO₂ nanoparticles is important to achieve a good electronic coupling between these two materials.

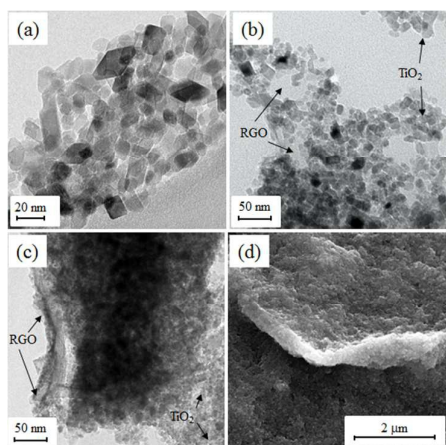


Fig. 1. HRTEM images of the powders of (a) TiO₂ particles, (b,c) TiO₂/RGO_(5%) nanocomposite and FEG-SEM image of the (d) powder TiO₂/RGO_(5%) nanocomposite.

The XRD patterns obtained for the TiO₂ and TiO₂/RGO_(5%) films and powder TiO₂/RGO_(5%) nanocomposite are presented in Fig. 2(a). The diffractograms also include the information of the Joint Committee on Powder Diffraction Standards (JCPDS) for anatase and rutile phases, 21-1272 and 21-1276, respectively. The Raman spectra obtained for the TiO₂ and TiO₂/RGO_(5%) films are presented in Fig. 2(b).

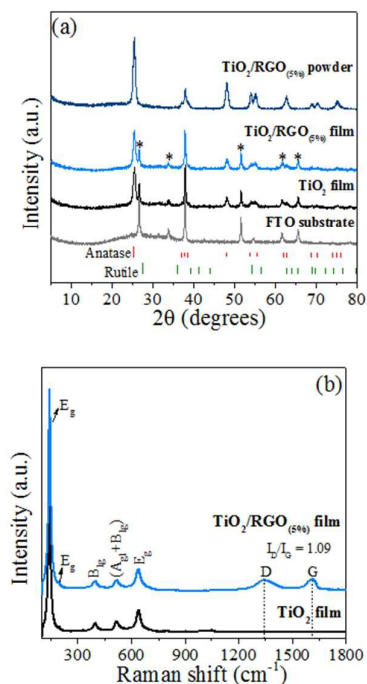


Fig. 2. (a) XRD patterns for the FTO substrate, TiO₂, TiO₂/RGO_(5%) films and powder TiO₂/RGO_(5%) nanocomposite. (b) Raman spectra for the TiO₂ and TiO₂/RGO_(5%) films.

The XRD pattern of the TiO₂/RGO_(5%) nanocomposite (powder) showed the presence of TiO₂ crystalline structure, predominantly the anatase allotropic form.³⁴ This information can also be observed in the TiO₂ and TiO₂/RGO_(5%) films but, the signs are less intense. The diffraction peaks at asterisk (*) correspond to crystalline phases of the FTO substrate. Comparison of the XRD diffraction peaks for the TiO₂/RGO_(5%)

composite and the pure TiO₂ films demonstrates that the RGO presence did not change the TiO₂ preferential crystal orientations. The typical diffraction peaks of carbon species, observed at 2θ = 25° in Fig. S5(a) (Supporting Information), are not observed in the composite, probably due to the relatively low RGO amount.³⁵

The Raman results showed specific vibration modes located around 150 cm⁻¹ (E_g), 200 cm⁻¹ (E_g), 400 cm⁻¹ (B_{1g}), 510 cm⁻¹ (B_{1g} + A_{1g}) and 630 cm⁻¹ (E_g) indicating the presence of anatase phase.³⁶ No peak assigned to rutile or brookite phase was observed, which was consistent with the XRD results. For the TiO₂/RGO_(5%) film, the two additional prominent peaks centered at 1324 cm⁻¹ (D band) and 1600 cm⁻¹ (G band) are also observed in the Raman spectrum, suggesting that the structure of RGO was maintained in the composite. Furthermore, an I_D/I_G ratio of 1.09, higher than that of RGO-hydrothermal sample (I_D/I_G = 1.02) (see Fig. S5(b) in the Supporting Information) was observed, suggesting a structural disorder related to the strong interaction between TiO₂ nanoparticles and RGO sheets after the reduction process by the hydrothermal method.³⁷

Fig. 3 shows images of the electrodes surface obtained by optical microscopy and FEG-SEM. While a transparent film was obtained from deposition of the pristine TiO₂ suspension on glass-FTO, a dark film resulted from the TiO₂/RGO_(5%) suspension (Fig.3(a)). Films with different TiO₂/RGO relative amounts were obtained from suspensions prepared by the mixture of pristine TiO₂ and TiO₂/RGO_(5%) suspensions; the images clearly shows that the composite films become darker with increasing the relative RGO concentration. Furthermore, different morphology can be observed for the films of TiO₂ and TiO₂/RGO composites. The images of all the nanocomposites films are available in Fig. S7 in the Supporting Information. The surface and cross-section images (Fig. 3(f-g)) show that the TiO₂/RGO_(5%) film has a high porosity, interconnected pores and thickness around 5.3 μm.

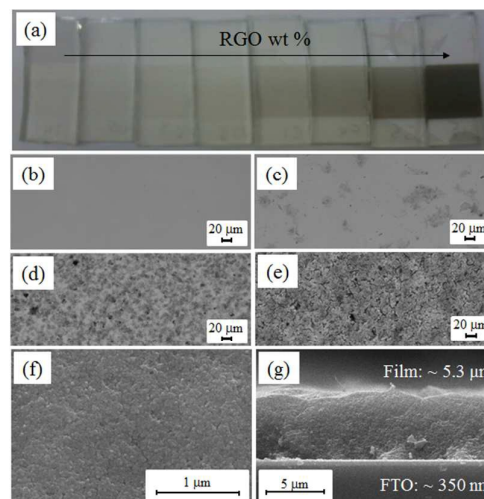


Fig. 3. (a) Photography of the TiO₂ and TiO₂/RGO films. Optical microscopy images of the (b) TiO₂, (c) TiO₂/RGO_(0.1%), (d) TiO₂/RGO_(2%) and (e) TiO₂/RGO_(5%) films. FEG-SEM images of the (f) surface and (g) cross-section of the TiO₂/RGO_(5%) film.

Fig. 4 shows the UV-visible absorption spectra of the TiO_2 and $\text{TiO}_2/\text{RGO}_{(0.1\%)}$, $\text{TiO}_2/\text{RGO}_{(2\%)}$ and $\text{TiO}_2/\text{RGO}_{(5\%)}$ films.

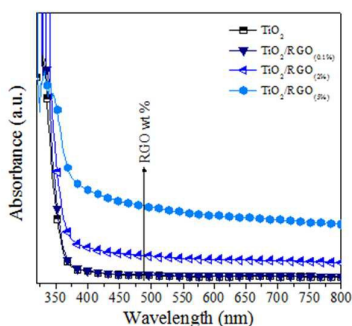


Fig. 4. UV-visible absorption spectra for the TiO_2 , $\text{TiO}_2/\text{RGO}_{(0.1\%)}$, $\text{TiO}_2/\text{RGO}_{(2\%)}$ and $\text{TiO}_2/\text{RGO}_{(5\%)}$ films.

A significant increase in the absorption at wavelengths shorter than 400 nm is assigned to the TiO_2 (~ 3.2 eV).³⁸ For the composites, the light absorption remains unchanged for RGO relative concentration < 1.0 wt %. On the other hand, there is a marked increase in the light absorption intensity in whole region investigated when the RGO concentration is greater than 1.0 wt %. In this case, the light scattering must also be considered mainly in the visible and near-infrared regions. The films become darker and this behavior will have an important implication in the photoelectrochemical response of these films, as it will be discussed in the last section. Tauc plots were used to determine the optical band gap in the films. The results showed that the addition of RGO decreases the band gap energy (E_g) from 3.6 eV (pristine TiO_2) to 3.4 eV (sample with 5.0 wt% of RGO). Such small variation, although positive, is not expected to play the major role in the photocurrent values.

Transient absorption spectroscopy studies of the TiO_2/RGO films

TAS measurements were performed to study the charge carrier dynamics (hole and electrons) after Nd:YAG laser excitation ($350 \mu\text{J cm}^{-2}$) in the ultraviolet region (355 nm) for the TiO_2 and TiO_2/RGO composites with RGO relative concentration of 0.1, 2 and 5 wt%. Fig. 5(a) and 5(b) shows the spectra obtained using the probe wavelengths at 460 nm (mainly photohole absorption) and 900 nm (mainly photoelectron absorption).

The observed transient absorption decays in the TiO_2 and TiO_2/RGO films are attributed to electron-hole recombination when the experiments are carried out under nitrogen in the absence of any chemical scavengers. Such behavior was also observed by Tang *et al.*³⁹ when studying the dynamics of the charge carriers in the nitrogen-doped- TiO_2 (nc-N- TiO_2) films. In all nanocomposite films containing RGO sheets, we observe an increase in the amplitude of the long lived 460 nm (photoholes) signals and also an increase in the amplitude of the long lived 900 nm (photoelectrons) signals in comparison with the pristine TiO_2 film. The optical density variation (ΔOD) observed is proportional to the number of charge carriers photogenerated and it is significantly larger for the

nanocomposites than the pristine TiO_2 films. This is a strong indication of a decrease of the charge recombination.

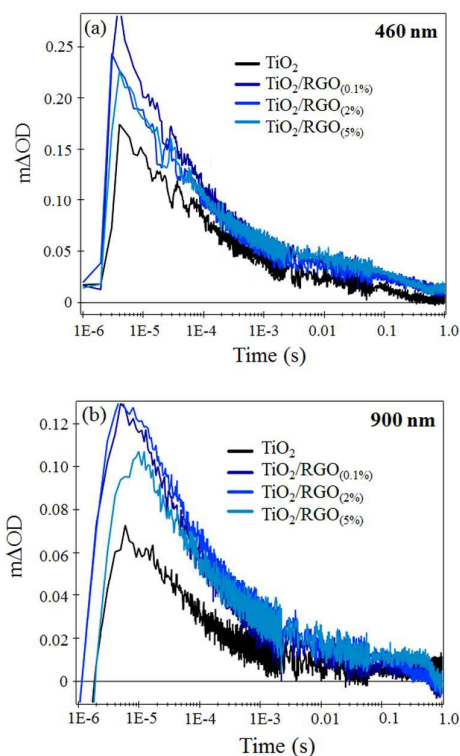


Fig. 5. Transient absorption spectra of (a) photoholes (460 nm) and (b) photoelectrons (900 nm) in TiO_2 , $\text{TiO}_2/\text{RGO}_{(0.1\%)}$, $\text{TiO}_2/\text{RGO}_{(2\%)}$ and $\text{TiO}_2/\text{RGO}_{(5\%)}$ films after Nd:YAG laser excitation, in the ultraviolet region (355 nm), in nitrogen atmosphere and in the absence of chemical scavengers.

The increase in the yield of holes is clear: considering the RGO sheets as electron acceptors, the charge recombination reaction between electrons and holes is minimized. In addition. The origin of the increase in the 900 nm signal is less clear and may derive from absorption of RGO electrons.

According to Meng *et al.*⁴⁰, which used TAS as additional tool to understand the photocatalytic improvement towards water oxidation in $\text{TiO}_2/\alpha\text{-Fe}_2\text{O}_3$ composite, the mechanism is associated to mobile electrons which are initially created in semiconductor and quickly transfer to the RGO sheet, where they diffuse into trap states in the RGO on a time scale of picoseconds. These trapped electrons reach the photoelectrode leading to an increase in the photocurrent.

Photoelectrochemical studies of the TiO_2/RGO films

Pristine TiO_2 and TiO_2/RGO films were employed as photoanodes in photoelectrochemical water splitting studies in a $0.5 \text{ mol L}^{-1} \text{ H}_2\text{SO}_4$ medium. The cyclic voltammograms, obtained in the dark and under illumination (100 mW cm^{-2} , AM 1.5G), through the electrolyte-electrode interface (EE), are shown in Fig. 6.

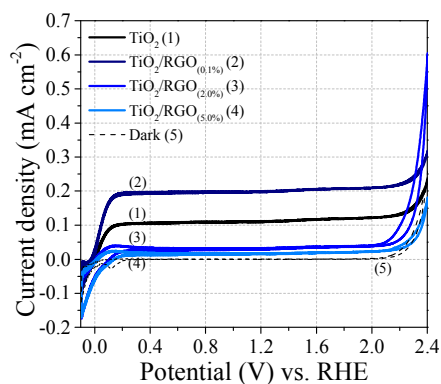


Fig. 6. Cyclic voltammograms obtained using the TiO_2 , $\text{TiO}_2/\text{RGO}_{(0.1\%)}$, $\text{TiO}_2/\text{RGO}_{(2\%)}$ and $\text{TiO}_2/\text{RGO}_{(5\%)}$ films as photoanodes in $0.5 \text{ mol L}^{-1} \text{ H}_2\text{SO}_4$, in the dark and under illumination.

In the wide potential range (0.4 to $2.4 V_{\text{RHE}}$), only a well-defined peak at ca. $-0.29 V_{\text{RHE}}$ is observed during the anodic sweep, that can be attributed to the oxidation of Ti(III) (hydr)oxide species ($>\text{Ti(OH)}$) in TiO_2 surface. During cathodic sweep, a reduction peak of the Ti(IV) (hydr)oxide species ($>\text{Ti(OH)}_2$) was also observed in potential lower than $0.06 V_{\text{RHE}}$ (see Fig. S9 in the Supporting Information).⁴¹ In the dark, the electrodes exhibited a very small capacitive current and for potential greater than $2.0 V_{\text{RHE}}$, the current is related to the oxygen evolution reaction (OER). Furthermore, it was also observed a well-defined peak at around $0.09 V_{\text{RHE}}$ during the cathodic sweep. The presence of this peak is widely discussed in the literature and it has been associated with the reduction of species at surface states located below the semiconductor conduction band, mainly due to the presence of electronic traps in the films. In potential below $0 V_{\text{RHE}}$, it also occurs the hydrogen evolution reaction (HER).⁴²

In the illumination conditions, as expected for n-type semiconductor electrodes, all the films showed an anodic photocurrent. According to Fig. 5(b), the photocurrent is directly dependent on the RGO concentration in the TiO_2 composite electrode. At $1.23 V_{\text{RHE}}$ (standard potential for OER) for the pristine TiO_2 electrode, the photocurrent corresponds to 0.11 mA cm^{-2} ; for composite electrodes, it increased with RGO relative concentration and the maximum value 0.20 mA cm^{-2} is observed for the composite containing 0.1 wt\% of RGO. The photocurrent declines sharply to 0.02 mA cm^{-2} with the $\text{TiO}_2/\text{RGO}_{(5\%)}$ film. The variation of photocurrent density values (at $1.23 V_{\text{RHE}}$) with the relative concentration of RGO in the TiO_2/RGO films electrodes is shown in Fig. S11 in the Supporting Information. The $\text{TiO}_2/\text{RGO}_{(0.1\%)}$ electrode has a maximum IPCE_(350nm) around 18% (see Fig. S12 in the Supporting Information), which is higher in comparison to other electrodes.

It is noteworthy that the onset potential ($\sim 0 V_{\text{RHE}}$) of all voltammograms did not change and so it is possible to discard any catalytic effect of the RGO sheets. It is very important to emphasize that these measurements were also repeated using the same photoelectrodes and experimental conditions, but with the use of a UV blocking filter ($< 400 \text{ nm}$). The

voltammograms profiles for all photoelectrodes were similar to the results obtained in the dark (compare the Fig. S10(a) and Fig. S13 in the Supporting Information). Thus, we can discard the RGO sheets, at least in our work, is acting as sensitizers in the TiO_2 film. Kumar *et al.*⁴³ have calculated the work function of rGO sheets as a function of the oxygen concentration. Thus, we expect that the work function for our sample is about 5.4 eV . The energy level of conduction band of TiO_2 is about 4.4 eV .⁴⁴ This is additional information that the energy levels do not allow electron transfer from the RGO to the conduction band of the titania film. However, in a recent report, Bharad *et al.*⁴⁵ reported a mechanism for water splitting reactions based on TiO_2 sensitization by RGO and N-doped RGO. It is clear that this subject needs a more deep investigation in order to check the feasibility of electron transfer from the graphene-based materials to titania films.

The photoresponse ability and long-term stability of the same photoelectrodes were determined using chronoamperometric measurements under potentiostatic control at $1.23 V_{\text{RHE}}$, as shown in Fig. 7. In general, the photoelectrodes exhibited a prompt photo-response under intermittent irradiation with high reproducibility during numerous ON/OFF cycles, as well as good electrochemical stability during continuous irradiation for 1 h . It is noteworthy that the photocurrent density values obtained by Chronoamperometry were very similar to the Cyclic Voltammetry.

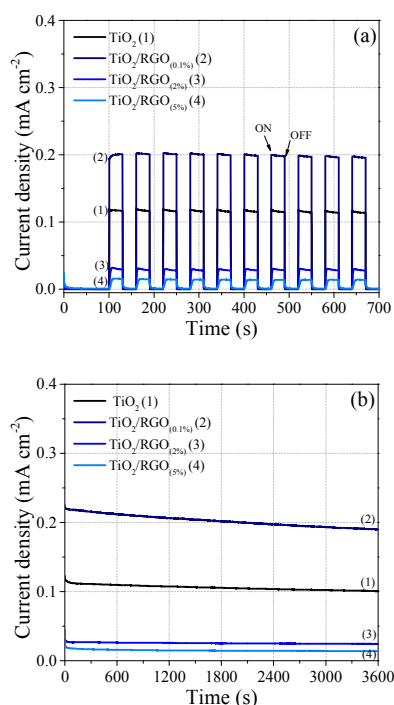


Fig. 7. Time-dependent photocurrent density under potentiostatic control at $1.23 V_{\text{RHE}}$ under intermittent irradiation using a manual chopper with intervals of 30 s in the dark and 30 s under irradiation (a) and under continuous irradiation (b) for the TiO_2 , $\text{TiO}_2/\text{RGO}_{(0.1\%)}$, $\text{TiO}_2/\text{RGO}_{(2\%)}$ and $\text{TiO}_2/\text{RGO}_{(5\%)}$ photoelectrodes in $0.5 \text{ mol L}^{-1} \text{ H}_2\text{SO}_4$.

The electrochemical and photoelectrochemical properties of these electrodes were also investigated by electrochemical impedance spectroscopy (EIS) measurements, carried out in H_2SO_4 aqueous solution at open circuit potential (V_{OC}), in the dark and under illumination. Fig. 8 presents the Nyquist and the Bode diagrams of the EIS data obtained for the TiO_2 and TiO_2/RGO photoelectrodes (represented by symbols), with their mathematical adjustment (represented by solid lines) obtained using the Boukamp software with the suggested equivalent circuit (inset in Fig. 8(a)). At V_{OC} , in the dark, all of these electrodes exhibited similar electrochemical impedance spectra, with high impedance values and undefined time constants (Fig 8(a) and 8(b)). Under illumination conditions, the general impedance value decreases considerably and a well-defined capacitive arc and two time constants can be displayed for all the photoelectrodes (Fig 8(c) and 8(d)). An equivalent circuit $R_s(Q_1(R_1(R_2C_2)))$ has been proposed for fitting the EIS data.^{15, 46, 47} All the adjustments have been made in the frequency range from 10 kHz to 0.1 Hz, due to the high dispersion of the data.

The proposed equivalent circuit (inset in Fig. 8(a)) considers a series resistance element (R_s), which includes the FTO resistance, the resistance related to the ionic conductivity of the electrolyte and the external contact resistance. The semiconductor|electrolyte interface can be represented by the capacitance at the Helmholtz layer (Q_1) on the electrolyte side and charge transfer resistance (R_1). The electron transport in the semiconductor bulk can be represented by the resistance (R_2) and the capacitance (C_2) at the TiO_2 surface states. The contribution of the RGO sheets on the TiO_2 surface can also be visualized by these two parameters. Moreover, in photoelectrodes formed by nanostructured semiconductors, the capacitance is commonly well represented by a CPE, which admittance depends on the parameters Y_0 and n (n is a constant ranging from $0 \leq n \leq 1$). In this case, the semiconductor electrode|electrolyte interface cannot be represented by simple circuits such as RC or R(RC), then, the resultant capacitance should not vary with applied potential, as assumed by Mott-Schottky relationship.^{15, 46, 47} The parameters obtained by fitting the EIS spectra with the equivalent circuit depicted in Fig. 7(a) are presented in Table 1.

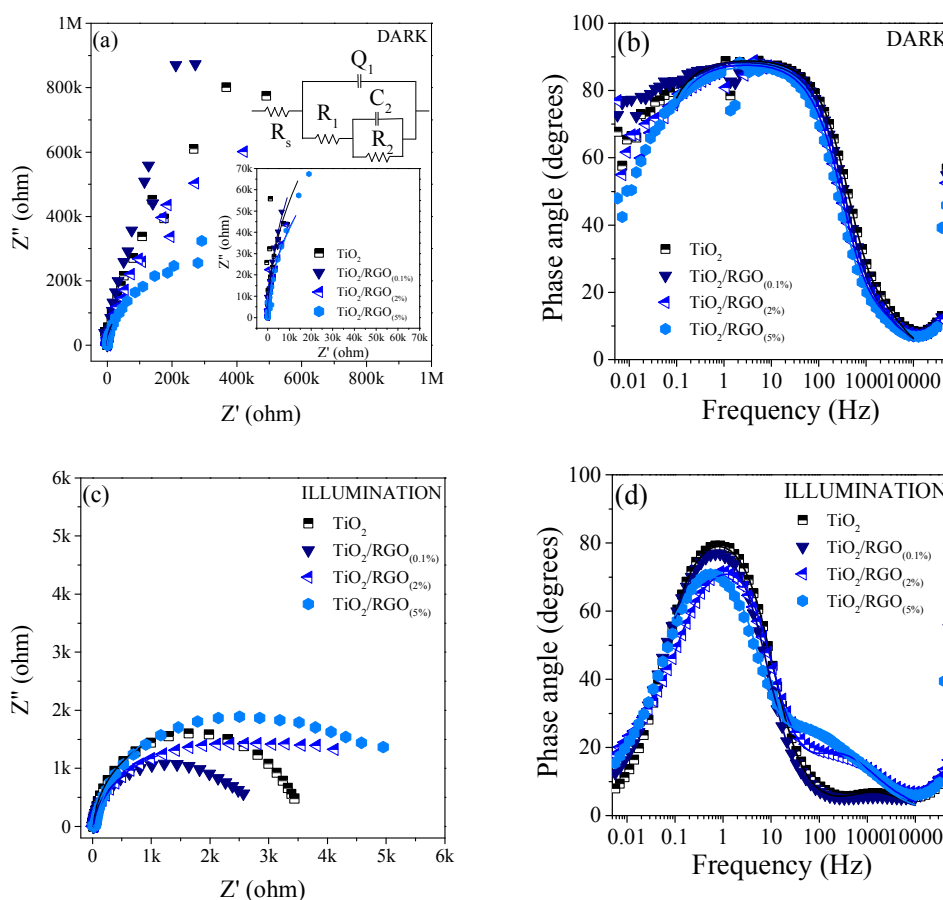


Fig. 8. (a) (b) Nyquist and (c) (d) Bode (phase angle versus frequency) diagrams of the EIS data obtained for the TiO_2 , $\text{TiO}_2/\text{RGO}(0.1\%)$, $\text{TiO}_2/\text{RGO}(2\%)$ and $\text{TiO}_2/\text{RGO}(5\%)$ photoelectrodes at open circuit potential, in 0.5 mol L⁻¹ H_2SO_4 in the dark (a) (b) and under illumination (c) (d). The symbols correspond to the experimental data and solid lines represent the fits obtained using the Boukamp software. The equivalent circuit inserted in Fig. 8(a).

The circuit elements values obtained in the dark are similar among the photoelectrodes, with R_s of ca. 14 Ω , capacitances (Q_1 and C_2) of ca. 15 μF and resistances (R_1 and R_2) of 10 Ω and 312 $\text{k}\Omega$ on average, respectively. Under illumination, the $\text{TiO}_2/\text{RGO}_{(0.01 \text{ to } 0.1\%)}$ electrodes showed R_1 (5.3 to 4.8 Ω) and R_2 (3.0 to 2.4 $\text{k}\Omega$) values lower than the pure TiO_2 electrode ($R_1 = 5.8 \Omega$ and $R_2 = 689 \text{ k}\Omega$). The capacitance values ($Q_1 \sim 316 \mu\text{F}$ and $C_2 \sim 1010 \mu\text{F}$) were higher compared to the

pristine TiO_2 electrode ($Q_1 = 166 \mu\text{F}$ and $C_2 = 689 \mu\text{F}$). This behavior indicates a higher charge accumulation at the interface and a faster electron transport, associated to the presence of the RGO.

Note that the low concentration of RGO in the TiO_2 film (< 0.1 wt %) does not significantly change the light absorption (see Fig. S8 in the Supporting Information).

Table 1. Parameters obtained by fitting the impedance spectra of the TiO_2 and TiO_2/RGO photoelectrodes in 0.5 mol L⁻¹ H₂SO₄, using the equivalent circuit $R_s(Q_1(R_1(R_2C_2)))$.

	Photoelectrodes	χ^2 (10 ⁻³)	R_s (Ω)	Q_1		R_1 (Ω)	R_2 ($\text{k}\Omega$)	C_2 (μF)
				Y_0 ($\mu\text{F s}^{n-1}$)	n			
DARK	TiO_2	6.0	12	13	0.99	11	324	11
	$\text{TiO}_2/\text{RGO}_{(0.01\%)}$	0.5	12	15	0.99	11	291	16
	$\text{TiO}_2/\text{RGO}_{(0.05\%)}$	4.6	15	11	0.99	8.8	417	16
	$\text{TiO}_2/\text{RGO}_{(0.1\%)}$	0.3	13	14	0.98	8.9	409	13
	$\text{TiO}_2/\text{RGO}_{(0.5\%)}$	0.6	13	16	0.98	10	383	14
	$\text{TiO}_2/\text{RGO}_{(1\%)}$	0.2	16	16	0.97	8.7	236	15
	$\text{TiO}_2/\text{RGO}_{(2\%)}$	0.4	14	16	0.97	9.8	212	14
	$\text{TiO}_2/\text{RGO}_{(5\%)}$	0.8	16	16	0.95	8.6	223	16
ILLUMINATION	TiO_2	0.2	14	166	0.78	5.8	3.6	689
	$\text{TiO}_2/\text{RGO}_{(0.01\%)}$	0.4	14	223	0.75	5.3	3.0	1083
	$\text{TiO}_2/\text{RGO}_{(0.05\%)}$	0.2	14	320	0.72	5.1	2.6	1218
	$\text{TiO}_2/\text{RGO}_{(0.1\%)}$	0.2	13	316	0.74	4.8	2.4	1010
	$\text{TiO}_2/\text{RGO}_{(0.5\%)}$	0.2	12	317	0.72	6.2	2.2	835
	$\text{TiO}_2/\text{RGO}_{(1\%)}$	0.3	15	337	0.70	14	2.4	451
	$\text{TiO}_2/\text{RGO}_{(2\%)}$	0.6	14	363	0.70	26	3.4	358
	$\text{TiO}_2/\text{RGO}_{(5\%)}$	1.3	14	471	0.68	63	6.2	367

* Fitting performed with the Boukamp software. The symbols R, C and Q account for resistance, capacitance and constant phase element (CPE), respectively.

On the other hand, the RGO concentrations above 0.5 wt % in the TiO_2 films, the photocurrent density values decrease and many factors may be related to this process. Under illumination, the $\text{TiO}_2/\text{RGO}_{(0.5 \text{ to } 5\%)}$ electrodes showed increasing values of R_1 and R_2 : 6.2 to 63 Ω and 2.2 to 6.2 $\text{k}\Omega$, respectively. In addition, there was a marked decrease in the values in one of the capacitances (C_2), from 835 to 367 μF . This can be directly related to the presence of agglomerations of RGO sheets that blocks the light absorption in the TiO_2 nanoparticles. The light-block effect contributes to the decay of the photocurrent density values, corroborating with the EIS data.

As the amount of RGO increases, charge recombination becomes more important and this can explain our best result obtained by the films containing 0.1 wt % of RGO. Besides, as the concentration of RGO increases, the films become darker and this seems to affect negatively the charge generation. As shown previously in Fig. 4, as the content of the RGO increases, the light absorption by the titania nanoparticles is compromised, decreasing the photoactivity towards water oxidation and also the charge generation. It is important to

point out the correspondence between the TAS and the photoelectrochemical studies. The sample that gave rise to the best performance in the water oxidation process ($\text{TiO}_2/\text{RGO}_{(0.1\%)}$) also originated the highest yield for both charge carriers.

Conclusions

Although several reports of the photocatalytic effect and water splitting reactions at the surface of TiO_2/RGO nanocomposite have been published in the last years, a clear understanding of the RGO role is missing. For instance, the sensitization effect of RGO in the titania film was not observed in our work. Besides, the energy levels of both materials do not allow charge transfer from the RGO to the titania conduction band. However, the opposite can be accomplished. In the photoelectrochemical water splitting investigation, the $\text{TiO}_2/\text{RGO}_{(0.1\%)}$ photoelectrodes showed the highest photocurrent density value (0.20 mA cm⁻² at 1.23 V_{RHE}) compared to other electrodes, with an increase of 78 % in relation to the pristine TiO_2 films (0.11 mA cm⁻² at 1.23 V_{RHE}).

However, at higher concentrations (0.5 to 5.0 wt %), the photocurrent density values sharply decreases, probably due to the darkening and the agglomerations of RGO sheets in these films, which deteriorated the electrical parameters as seen by EIE. The TAS results indicated an increase in lifetime and yield of both photogenerated holes and electrons. Interesting, the TiO₂/RGO_(0.1%) films was the one, which exhibited the best charge generation upon excitation, corroborating with the photoelectrochemical studies. We proposed that in films with lower concentration (< 0.1 wt %), the positive effect of the RGO sheets is due to their ability into accept and transfer electrons from the TiO₂. The immediate consequence is a decrease in charge recombination, observed by the increase in the photogeneration of holes and electrons in TAS decays and a significant improvement in photocurrent density in the photoelectrochemical water splitting.

Acknowledgements

The authors thank LNNano/LNLS for the FEG-SEM and HRTEM images, Inmetro for the XPS analysis, and INEO, CNPq and FAPESP (fellowship 2010/18656-1 and 2011/51593-6) for financial support.

Notes and references

1. A. Fujishima and K. Honda, *Nature*, 1972, **238**, 37-38.
2. M. G. Walter, E. L. Warren, J. R. McKone, S. W. Boettcher, Q. X. Mi, E. A. Santori and N. S. Lewis, *Chem Rev*, 2010, **110**, 6446-6473.
3. M. Ni, M. K. H. Leung, D. Y. C. Leung and K. Sumathy, *Renew Sust Energ Rev*, 2007, **11**, 401-425.
4. H. Fakhouri, J. Pulpitel, W. Smith, A. Zolfaghari, H. R. Mortaheb, F. Meshkini, R. Jafari, E. Sutter and F. Arefi-Khonsari, *Appl Catal B-Environ*, 2014, **144**, 12-21.
5. G. J. Ai, R. Mo, H. Xu, Q. Chen, S. Yang, H. X. Li and J. X. Zhong, *J Power Sources*, 2015, **280**, 5-11.
6. A. M. Mohamed, A. S. Aljaber, S. Y. AlQaradawi and N. K. Allam, *Chem Commun*, 2015, **51**, 12617-12620.
7. J. Z. Su and L. J. Guo, *Rsc Adv*, 2015, **5**, 53012-53018.
8. C. Fabrega, T. Andreu, A. Tarancon, C. Flox, A. Morata, L. Calvo-Barrio and J. R. Morante, *Int J Hydrogen Energ*, 2013, **38**, 2979-2985.
9. S. H. Liu and H. R. Syu, *Appl Energ*, 2012, **100**, 148-154.
10. B. O'Regan, J. Moser, M. Anderson and M. Grätzel, *J. Phys. Chem.*, 1990, **94**, 8720-8726.
11. A. Westwood and R. Leary, *Carbon*, 2011, **49**, 741-772.
12. K. Dai, T. Y. Peng, D. N. Ke and B. Q. Wei, *Nanotechnology*, 2009, **20**, 125603.
13. Y. Cong, X. K. Li, Z. J. Dong, G. M. Yuan, Z. W. Cui and J. Zhang, *Mater Lett*, 2015, **138**, 200-203.
14. M. X. Sun, X. Q. Ma, X. Chen, Y. J. Sun, X. L. Cui and Y. H. Lin, *Rsc Adv*, 2014, **4**, 1120-1127.
15. K. Ranganathan; A. Morais; I. Nongwe; C. Longo; A. F. Nogueira; and N. J. Coville, *J Mol Catal a-Chem*, 2016, - aceito para publicação.
16. A. de Morais, L. M. D. Loiola, J. E. Benedetti, A. S. Goncalves, C. A. O. Avellaneda, J. H. Clerici, M. A. Cotta and A. F. Nogueira, *J Photoch Photobio A*, 2013, **251**, 78-84.
17. Q. J. Xiang, J. G. Yu and M. Jaroniec, *Chem Soc Rev*, 2012, **41**, 782-796.
18. S. F. Pei and H. M. Cheng, *Carbon*, 2012, **50**, 3210-3228.
19. X. Y. Zhang, H. P. Li, X. L. Cui and Y. H. Lin, *J Mater Chem*, 2010, **20**, 2801-2806.
20. B. W. Wang, Q. M. Sun, S. H. Liu and Y. P. Li, *Int J Hydrogen Energ*, 2013, **38**, 7232-7240.
21. F. Y. Pei, Y. L. Liu, L. Zhang, S. P. Wang, S. G. Xu and S. K. Cao, *Mater Res Bull*, 2013, **48**, 2824-2831.
22. F. Y. Pei, G. L. Liu, S. G. Xu, J. Lu, C. X. Wang and S. K. Cao, *Int J Hydrogen Energ*, 2013, **38**, 2670-2677.
23. Y. H. Ng, I. V. Lightcap, K. Goodwin, M. Matsumura and P. V. Kamat, *J Phys Chem Lett*, 2010, **1**, 2222-2227.
24. N. J. Bell, H. N. Yun, A. J. Du, H. Coster, S. C. Smith and R. Amal, *J Phys Chem C*, 2011, **115**, 6004-6009.
25. H. Li and X. L. Cui, *Int J Hydrogen Energ*, 2014, **39**, 19877-19886.
26. J. E. Benedetti, D. R. Bernardo, A. Morais, J. Bettini and A. F. Nogueira, *Rsc Adv*, 2015, **5**, 33914-33922.
27. B. M. Almeida, M. A. Melo, J. Bettini, J. E. Benedetti and A. F. Nogueira, *Appl Surf Sci*, 2015, **324**, 419-431.
28. A. Morais, J. P. C. Alves, F. A. S. Lima, M. Lira-Cantu and A. F. Nogueira, *J Photon Energy*, 2015, **5**, 057408.
29. N. L. Yang, J. Zhai, D. Wang, Y. S. Chen and L. Jiang, *Acs Nano*, 2010, **4**, 887-894.
30. T. F. Yeh, J. Cihlar, C. Y. Chang, C. Cheng and H. S. Teng, *Mater Today*, 2013, **16**, 78-84.
31. M. Q. Yang and Y. J. Xu, *J Phys Chem C*, 2013, **117**, 21724-21734.
32. Y. H. Zhang, N. Zhang, Z. R. Tang and Y. J. Xu, *Acs Nano*, 2012, **6**, 9777-9789.
33. A. J. Du, Y. H. Ng, N. J. Bell, Z. H. Zhu, R. Amal and S. C. Smith, *J Phys Chem Lett*, 2011, **2**, 894-899.
34. Y. H. Zhang, Z. R. Tang, X. Z. Fu and Y. J. Xu, *Acs Nano*, 2010, **4**, 7303-7314.
35. Y. H. Zhang, Z. R. Tang, X. Fu and Y. J. Xu, *Acs Nano*, 2011, **5**, 7426-7435.
36. S. D. Perera, R. G. Mariano, K. Vu, N. Nour, O. Seitz, Y. Chabal and K. J. Balkus, *Acs Catal*, 2012, **2**, 949-956.
37. B. T. Liu, Y. J. Huang, Y. Wen, L. J. Du, W. Zeng, Y. R. Shi, F. Zhang, G. Zhu, X. H. Xu and Y. H. Wang, *J Mater Chem*, 2012, **22**, 7484-7491.
38. J. J. Fan, S. W. Liu and J. G. Yu, *J Mater Chem*, 2012, **22**, 17027-17036.
39. J. W. Tang, A. J. Cowan, J. R. Durrant and D. R. Klug, *J Phys Chem C*, 2011, **115**, 3143-3150.
40. F. K. Meng, J. T. Li, S. K. Cushing, J. Bright, M. J. Zhi, J. D. Rowley, Z. L. Hong, A. Manivannan, A. D. Bristow and N. Q. Wu, *Acs Catal*, 2013, **3**, 746-751.
41. F. Y. Oliva, L. B. Avalle, E. Santos and O. R. Camara, *Journal of Photochemistry and Photobiology A-Chemistry*, 2002, **146**, 175-188.
42. T. Berger, D. Monllor-Satoca, M. Jankulovska, T. Lana-Villarreal and R. Gomez, *Chemphyschem*, 2012, **13**, 2824-2875.
43. P. V. Kumar, M. Bernardi and J. C. Grossman, *Acs Nano*, 2013, **7**, 1638-1645.
44. H. J. Tang, C. M. Hessel, J. Y. Wang, N. L. Yang, R. B. Yu, H. J. Zhao and D. Wang, *Chem Soc Rev*, 2014, **43**, 4281-4299.
45. P. A. Bharad, K. Sivarajani and C. S. Gopinath, *Nanoscale*, 2015, **7**, 11206-11215.
46. B. Klahr, S. Gimenez, F. Fabregat-Santiago, T. Hamann and J. Bisquert, *J Am Chem Soc*, 2012, **134**, 4294-4302.
47. T. Lopes, L. Andrade, F. Le Formal, M. Gratzel, K. Sivula and A. Mendes, *Phys Chem Chem Phys*, 2014, **16**, 16515-16523.

